Fast Computation of the No-Load Characteristic for Wound Field Synchronous Propulsion Motors

(Article begins on next page)

16 November 2024

Fast Computation of the No-Load Characteristic for Wound Field Synchronous Propulsion Motors

Federica Graffeo, *Member, IEEE*, Silvio Vaschetto, *Senior Member, IEEE*, Sandro Rubino, *Member, IEEE*, Alberto Tenconi, *Senior Member, IEEE*, and Andrea Cavagnino, *Fellow, IEEE*

Abstract—**Wound field synchronous machines are gaining attention as an interesting permanent magnet-free alternative for propulsion applications. The third degree of freedom introduced by the rotor current makes the electromagnetic design of these machines not trivial. Hence, dedicated and fast analysis tools are necessary to predict the machine behavior. This paper presents a fully analytical procedure for the computation of the no-load characteristic of salient-pole wound field synchronous machines. The procedure considers the iron saturation and includes the magnetic shunt of the stator slots. The distortion of the air gap flux density waveform introduced by the teeth saturation and the rotor saliency are considered. The procedure has been experimentally validated using a 4 poles, 100 kW peak power wound field synchronous motor.**

Index Terms—**Synchronous machines, wound field excitation, electromagnetic design, no-load characteristic, transportation electrification, propulsion motors.**

I. INTRODUCTION

IN the path towards propulsion decarbonization, electrical machines equipped with permanent magnets (PMs) are often considered the preferred solution for transportation electrification because of their high efficiency and superior power density compared to the other machine options [1]. Nonetheless, the use of rare-earth elements in the production of high energy PMs has raised concerns related to environmental, economic, technical, and social sustainability, driving towards alternative solutions [2], [3]. Wound Field Synchronous Machines (WFSMs), also known as electrically/externally excited synchronous machines, have recently gained attention as a promising PM-free motor alternative, as shown by recent automotive market trends [4]-[9]. One of the main characteristics of WFSMs is the controllability of the rotor current that allows a complete regulation of the excitation field,

which brings numerous advantages. For instance, high torques can be produced at low speeds by overloading both the stator and the rotor, avoiding excessive oversize of the inverter [10]. Wide constant power speed ranges can be achieved by properly adjusting the rotor current, while maintaining high efficiencies also at high speeds, where electric vehicles are frequently driven [7], [11]. Moreover, since the machine excitation can be removed in case of fault, concerns related to uncontrolled generation operations are avoided, guarantying an excellent fault mitigation capability, strictly requested by the aviation industry [12]. Furthermore, the field current can be regulated to achieve internal voltage values that exceed those at the machine terminals; consequently, the machine can be operated with a leading power factor. This possibility has been particularly interesting for large propulsion systems, such as in naval applications, as it allows using cost-effective load commutated power converters, as cycloconverters [13]-[15].

However, the presence of the rotor current introduces additional Joule losses in the machine. Although this may not have a significant impact on the machine efficiency, adequate cooling techniques may be necessary to extract the heat generated in the rotor. Moreover, the necessity to supply rotating parts probably represents the most limiting factor in WFSM's popularity [5]. This task has been historically accomplished through brushes and slip rings, causing concerns related to wear and reliability. However, this solution is currently used by some car manufacturers [16], proving the brush wear to be compatible with the maintenance needs of automotive applications. Anyway, wireless power transfer alternatives can also be used, as widely demonstrated in the context of aircraft on-board auxiliary generation [17]-[19].

The additional degree of freedom introduced by the rotor current significantly expands the design space, making the electromagnetic sizing of WFSM not trivial. Dedicated electromagnetic analysis tools have been proposed to facilitate the design of WFSMs. Examples are based on magnetic equivalent circuits [20], surrogate modeling or metamodeling approaches [21], analytical models [22], [23]. Analytical models commonly reach the best computational performance, but they usually rely on a certain number of assumptions to achieve closed-form formulations. However, they are a valuable tool in situations where symmetries can be exploited, as for the no-load characteristic computation, which represents a key step in both the analysis and the design of WFSMs [24].

In this scenario, the authors propose a fast computation of the no-load characteristic for wound field synchronous motors, through a self-consistent approach originally presented in [25]. In particular, the procedure is based on a comprehensive analytical computation scheme and considers the lamination saturation, the distortion of the air gap flux density waveform,

Fig. 1. Magnetic circuit along the *d*-axis [25].

Fig. 2. Scheme of no-load characteristic computation.

the slot shunt effect in presence of heavy saturation of the stator teeth, and the anisotropic structure of the salient poles. Thus, the paper provides a significant contribution by collecting all the equations for computing the no-load characteristic of WFSMs into a single reference. The procedure is thoroughly explained and experimentally validated on a sample of the wound field motor equipping the Renault ZOE.

II. NO-LOAD COMPUTATION PROCEDURE

The no-load characteristic of wound field synchronous machines is the relation between the induced no-load voltage E_s and the rotor current I_r, at a given speed. This characteristic can be obtained by the curve of the fundamental flux density in the air gap $B_{g,1}$ for different values of the rotor ampere-turns AT_{tot} required for the no-load magnetization [26].

The computation of the function $B_{g,1}(AT_{tot})$ is based on the subdivision of the machine magnetic circuit along the *d*-axis into 5 different parts, as shown in Fig. 1: the air gap, the stator and rotor yoke, the stator teeth, and the rotor pole. The computational process is reported in Fig 2, where $B_{g,max}$ is the maximum value of the magnetic flux density in the air gap, AT_g and AT_t are the magnetomotive forces (MMF) drops in the air gap and stator teeth, respectively. The sum of the MMF drops in the air gap and stator teeth is called AT_{gt}.

As sketched in Fig 2, the procedure follows two different steps. In the first step, the MMF drops of the air gap and the stator teeth are computed for different values of the maximum magnetic flux density in the air gap, obtaining the curve $B_{g,max}(AT_{gt})$. The resulting curve is subsequently used in the second step to obtain the waveform of the magnetic flux density in the air gap, i.e. B_g as a function of the angular position α referred to the *d*-axis. The latter enables the computation of the fundamental value of the magnetic flux density in the air gap, as well as the remaining MMF drops (stator yoke, rotor pole and rotor yoke). The sum of all the MMF drops provides the value of the total ampere-turns AT_{tot} for a specific maximum magnetic flux density in the air gap. Under the assumption of a sinusoidal airgap MMF distribution, the function $B_{g,max}(AT_{gt})$ allows computing the fundamental airgap flux density B_{g1}. Repeating the computation for different values of $B_{g,max}$, the characteristic $\{AT_{tot}, B_{g1}\}$ is obtained, and thus $\{I_r, E_s\}$.
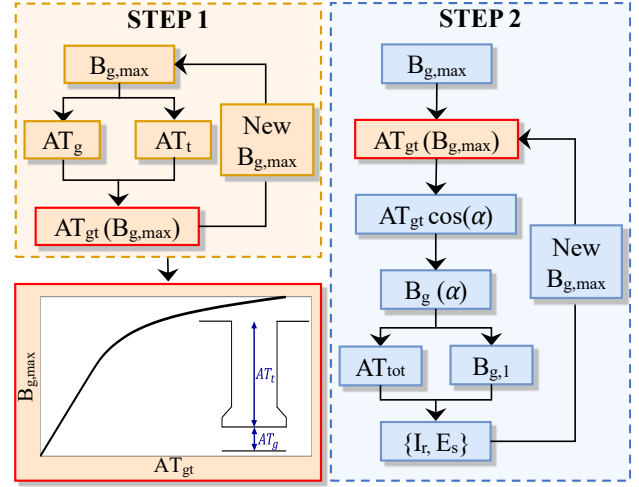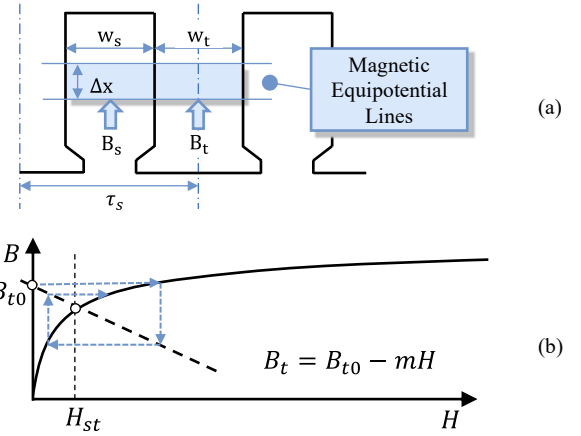
Fig. 3. The shunt effect of the slot (a), and the sketch for the teeth working point determination (b) [25].

A. Procedure assumptions

The procedure relies on the following assumptions:

- The airgap MMF distribution is considered sinusoidal.

- The distortion of the air gap flux density over the rotor pole shoe is solely due to the teeth saturation.

- The pole-to-pole leakage flux path is neglected.

B. STEP 1

1) *Air gap MMF Drop*

The air gap length of salient-pole WFSM is non-constant along the rotor external circumference [26]. Generally, it is shaped to be inversely proportional to the cosine of the angle α – see Fig. 1.

$$g(\alpha_m) = \frac{g_0}{\cos(p \cdot \alpha_m)} \tag{1}$$

$$AT_g = \frac{B_{g,max}}{\mu_0} \cdot k_c \cdot g_0 \tag{2}$$
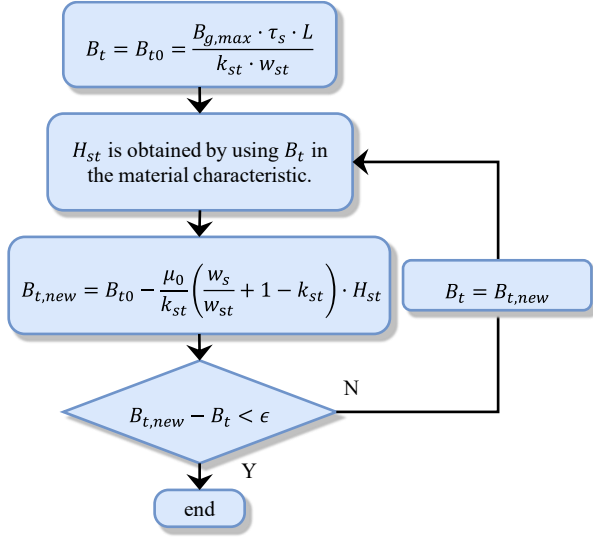
Fig. 4. Iterative procedure for the computation the magnetic flux density of the i-th tooth.

In (1) α_m is the mechanical angle from d-axis to q-axis, p is the number of pole pairs, and g_0 is the minimum air gap length. The MMF drop in the air gap can be computed as in (2), where k_c is the Carter factor computed for the average air gap length.

2) Stator teeth MMF Drop

The saturation of the stator teeth has a significant impact on the total amount of magnetizing ampere-turns. In light saturation conditions, it is generally assumed that the magnetic flux relative to one slot pitch is entirely funnelled through the teeth. As deductible by Fig. 3, the initial unsaturated value of the magnetic flux density B_{t0} in each tooth layer can be computed by (3) and (4), where τ_s is the slot pitch, and L is the axial length.

$$\Phi_{sp} = B_{g,max} \cdot \tau_s \cdot L \tag{3}$$

$$B_{t0} = \frac{\Phi_{sp}}{k_{st} \cdot w_t} \tag{4}$$

In strong saturation conditions, the amount of magnetic flux in the slot becomes non-negligible and the effective magnetic loading in the teeth should be evaluated by using the following iterative procedure. Firstly, the slot and the tooth are divided into N layers, as shown in Fig. 3a, and it is assumed that the equipotential lines of the magnetic field strength are parallel [27]. For each layer, the magnetic flux of both the stator tooth (5) and the stator slot (6) are computed.

$$\Phi_t = B_t \cdot L \cdot k_{st} \cdot w_t \tag{5}$$

$$\Phi_s = B_s \cdot L \cdot w_s + B_s \cdot L \cdot (1 - k_{st}) \cdot w_t \tag{6}$$

Where B_t and B_s are the magnetic flux density in the tooth and in the slot respectively, k_{st} is the lamination stack factor, w_t and w_s are the widths of the tooth and the slot respectively. In equation (6), the first term represents the flux shunt of the slot, while the second the flux shunt of the air between the lamination sheets.
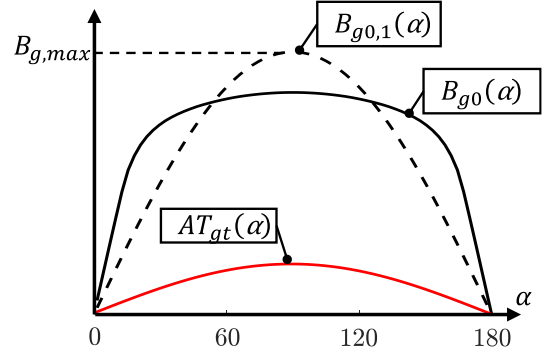

Fig. 5. Air gap flux density distortion [25].

The sum of the magnetic flux of the tooth and the slot is the magnetic flux relative to one slot pitch.

$$\Phi_{sp} = \Phi_t + \Phi_s \tag{7}$$

Substituting (4)-(6) in (7), the value of B_{t0} is:

$$B_{t0} = B_t + \frac{\mu_0}{\mu_{st}} \cdot \left(\frac{w_s}{w_t} + 1 - k_{st}\right) \cdot H_{st} = B_t + m \cdot H_{st} \tag{8}$$

In (8), H_{st} is the magnetic field assumed equal for both the tooth and the slot. The working point of the teeth is thus obtained by intersecting the iron magnetic characteristic with the line $B_{t0} - mH$, as expressed in (9) and shown in Fig. 3b.

$$\begin{cases} B_t = B(H) \\ B_t = B_{t0} - m \cdot H \end{cases} \tag{9}$$

Therefore, for a given value of $B_{g,max}$, the MMF drop in the i-th layer of the teeth is obtained as summarized in the scheme of Fig. 4, i.e. by implementing the following steps:

- The tooth and the slot are divided into N layers.

- The value of B_{t0} is computed using equation (3) and (4) and it is assumed as the starting value of the magnetic flux density in the tooth B_t.

- The value of H_{st} is obtained by using B_t in the material characteristic.

- The new value of B_t is computed through equation (8).

- If the new value differs from the previous one more than a fixed tolerance, the computation is repeated assuming the new value of B_t as starting value.

The MMF drop in the teeth is obtained by summing the MMF drop of each layer, as in (10), where H_i is the magnetic field of the i-th layer and Δx is the length of the layer.

$$AT_t(B_{g,max}) = \sum_{i=1}^{N} H_i \cdot \Delta x \tag{10}$$

By varying the value of $B_{g,max}$ the function $AT_t(B_{g,max})$ is obtained. The MMF drop AT_{gt} is therefore obtained by summing AT_g and AT_t, computed through (2) and (10), for different values of $B_{g,max}$. This allows for the construction of the characteristic $\{AT_{gt}, B_{g,max}\}$, necessary for the second step.
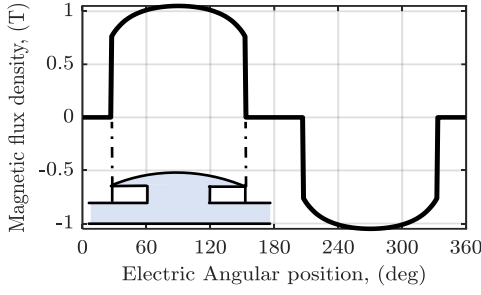
Fig. 6. Typical air gap flux density in the air gap [25].

C. STEP 2

1) Air gap flux density waveform

The computation of the MMF drop in the stator yoke, as well as in the remaining considered machine parts, requires the calculation of the waveform of the magnetic flux density in the air gap. The specific shape of the polar shoe given by (1) leads to a sinusoidal MMF distribution at the air gap. In saturation conditions, the waveform of the magnetic flux density produced by a sinusoidal MMF waveform is distorted along the air gap circumference, as shown in Fig. 5. It is assumed that the distortion is mainly caused by the teeth saturation, while the MMF drops in the stator and rotor yoke and in the pole do not affect the air gap flux density distortion. Therefore, considering a sinusoidal MMF at the air gap, its maximum value is obtained from the function $AT_{gt}(B_{g,max})$, for a given value of $B_{g,max}$. The function of the MMF in the air gap is thus built as in (11).

$$AT_{gt}(\alpha) = AT_{gt}(B_{g,max}) \cdot \cos(\alpha) \tag{11}$$

For the computation of the air gap flux density, it must be considered that its value in the area between two consecutive poles is nearly zero. Indeed, the presence of a large area of air in the q-axis causes the air gap flux density to decrease abruptly, as it can be appreciated in Fig. 6. Therefore, the air gap flux density can be modelled as a function of the angular variable α as in (12), valid under the assumption of neglecting the leakage flux from pole to pole.

$$B_g(\alpha) = \begin{cases} B_{g,0}(\alpha), & \alpha \le k_b \cdot \dfrac{\pi}{2} \\ 0 & , \quad \alpha > k_b \cdot \dfrac{\pi}{2} \end{cases} \tag{12}$$

Where k_b represents the percentage of polar pitch occupied by the pole head, and $B_{g,0}$ is the distorted air gap flux density distribution. The value of $B_{g,0}$ is determinable by means of the procedure shown in Fig. 7 [27]. Thus, the fundamental value of the obtained flux density is computed as in equation (13).

$$B_{g1} = \frac{4}{\pi} \int_0^{\pi/2} B_g(\alpha) \cdot \cos(\alpha) \, d\alpha \tag{13}$$

The computation of the integral is discretized by dividing half pole of the air gap into N_y pieces, hence the variable α is the angular position of the center of each piece. Therefore, it is possible to compute the fundamental value of the distorted magnetic flux density as in (14), being the discretization of equation (13).
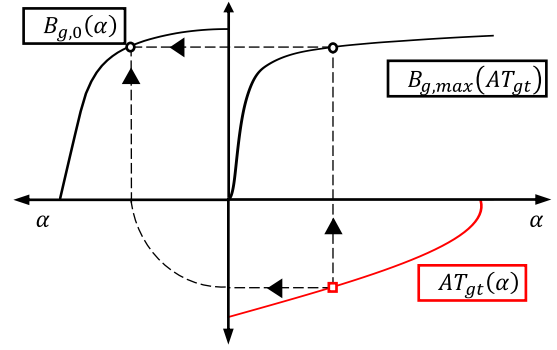
Fig. 7. Distorted air gap flux density computation [25].
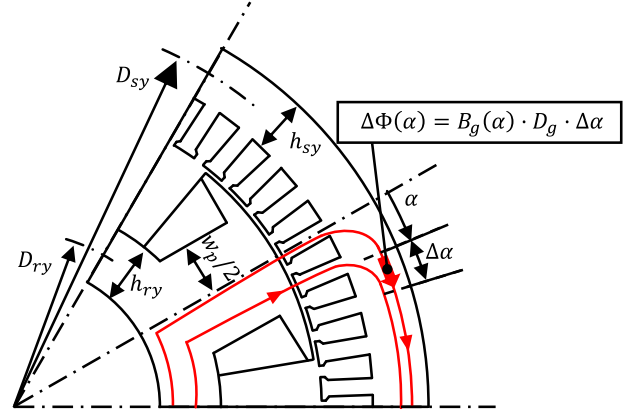
Fig. 8. Sketch for the stator yoke MMF computation [25].

$$B_{g1} = \frac{2}{N_y} \sum_{i=1}^{N_y} B_g(\alpha) \cdot \cos(\alpha_i) \tag{14}$$

2) Stator yoke MMF drop

In the stator yoke, the flux density takes the minimum value in the d-axis, and it progressively increases moving towards the q-axis, as understandable from Fig 8. Therefore, the air gap flux density in the stator yoke can be expressed as in (15), starting from the function of the magnetic flux density in the air gap, being D_g the diameter at the air gap and h_{sy} the stator yoke height.

$$B_{sy}(\alpha) = \int_0^\alpha B_g(\alpha) \cdot \frac{D_g}{2 \cdot h_{sy}} \cdot \frac{1}{k_{st} \cdot p} \cdot d\alpha \tag{15}$$

For a discrete variable α, the magnetic flux density in the yoke can be expressed as (16), where n_y is the number of yoke pieces for $\alpha = \alpha_i$.

$$B_{sy}(\alpha) = \sum_{i=1}^{n_y} B_g(\alpha_i) \cdot \frac{D_g}{2 \cdot h_{sy}} \cdot \frac{1}{k_{st} \cdot p} \cdot \Delta\alpha \tag{16}$$

Finally, the MMF drop in the stator yoke is computed as in (17), where D_{sy} is the diameter at the center of the yoke.

$$AT_{st}(B_{g,max}) = \sum_{i=0}^{N_y} H\left(B_{sy}(\alpha_i)\right) \cdot \frac{D_{sy}}{2p} \cdot \Delta\alpha \tag{17}$$

3) Rotor yoke and pole MMF drop

For what concerns the computation of the MMF drop in the rotor yoke and pole, a constant value of the magnetic flux is considered in both branches. Indeed, as shown in Fig. 8, due to the absence of the slots in the rotor, the whole magnetic flux flows through the rotor yoke and pole body. However, such assumption implies the approximation of neglecting the magnetic flux variation on the tooth body root where the magnetic flux funnels into the rotor pole body. The flux per pole must be introduced in order to compute the remaining rotor MMF drops, and it is obtained by integration of the magnetic flux density in the air gap over the polar pitch.

$$\Phi_p = 2 \cdot \sum_{i=1}^{N_y} B_g(\alpha_i) \cdot D_g \cdot L \cdot \frac{1}{2p} \cdot \frac{\pi}{2} \quad (18)$$

The values of the magnetic flux density in the rotor yoke and pole are computed as in equations (19) and (20) respectively.

$$B_{ry} = \frac{\Phi_p}{2} \cdot \frac{1}{h_{ry} \cdot L \cdot k_{st}} \quad (19)$$

$$B_p = \Phi_p \cdot \frac{1}{w_p \cdot L \cdot k_{st}} \quad (20)$$

From the magnetic curve of the material the magnetic field in the rotor yoke (H_{ry}) and in the pole (H_p) are obtained. Thus, it is possible to compute the MMF drops as in (21) and (22), considering D_{ri} is the inner rotor diameter, h_{ry} is the rotor yoke height, and l_p is the rotor pole length.

$$AT_{ry} = H_{ry} \cdot \frac{(D_{ri} + h_{ry}) \cdot \pi}{4p} \quad (21)$$

$$AT_p = H_p \cdot l_p \quad (22)$$

4) Total MMF drop & No-Load characteristic

Finally, for a given value of $B_{g,max}$, the total ampereturns required to magnetize the circuit in the d-axis is obtained by summing all the computed MMF drops of each considered machine part, as in (23).

$$AT_{tot} = AT_d + AT_t + AT_{sy} + AT_{ry} + AT_p \quad (23)$$

At this stage the characteristic $\{AT_{tot}, B_{g1}\}$ has been identified by varying the value of $B_{g,max}$ and following the proposed procedure. The curve must now be manipulated to obtain the no-load characteristic $\{E_s, I_r\}$. The rotor current value is simply obtained dividing the total ampereturns by the number of rotor turns N_r. The fundamental component of no-load voltage can be obtained from the fundamental component of the magnetic flux density in the air gap, as shown in (24). where E_s is expressed in rms, f is the electrical frequency, $k_{w,1}$ is the winding factor for the fundamental harmonic, N_s is the equivalent number of turns in series per phase of the stator.

$$E_s = \frac{2\pi}{\sqrt{2}} \cdot f \cdot k_{w,1} \cdot N_s \cdot \left(\frac{2}{\pi} \cdot \tau_p \cdot L \cdot B_{g1}\right) \quad (24)$$

III. VALIDATION OF THE PROCEDURE

The proposed method is initially validated by means of FEM simulations on three different machine geometries. Furthermore, the procedure is validated through experimental tests conducted on a salient-pole wound field synchronous motor used for traction applications. In both cases, the values of N and N_y are set to 100.

A. Validation with Finite Element Method

Three machines are used as reference for the results comparison, hereinafter WFSM1, WFSM2, and WFSM3, whose main characteristics are listed in Table I. The values of the parameters for WFSM1 and WFSM2 exhibit several differences, while the key distinction between WFSM2 and WFSM3 lies in the value of k_b. This deliberate contrast is intended to isolate and analyze the specific impact of this parameter on the procedure accuracy.

The no-load characteristics of the three WFSMs have been computed following the proposed procedure, with a resolution of 100 points and considering a maximum value for $B_{g,max}$ of 1.1 T. Subsequently, the three no-load characteristics have been obtained through FEM simulations of a single pole machine sector, using the finite element program FEMM [28]. In this case, the rotor winding has been supplied with 15 of the rotor currents obtained from the analytical procedure, in order to achieve the comparison in a reasonable computational time. For each rotor current, the value of the stator voltage has been obtained by getting the air gap magnetic flux density for a single rotor position and using its fundamental value in equation (24).

The obtained results are reported in Fig. 9-11 for the three machines. Specifically, Fig. 9a, Fig. 10a and Fig. 11a show the 2D sketch of the lamination geometry of the three motors. Figure 9b, Fig. 10b and Fig. 11b report the comparison of the analytically computed no-load characteristics with FEM simulations. The obtained values can be directly compared by looking at Table II-IV, which collect the no-load voltages for each rotor current, as well as the error between FEM and the analytical procedure. Finally, the left side of Fig. 9c, Fig. 10c and Fig. 11c compares the FEM and analytical air gap flux density curves for $B_{g,max} = 1\,T$, while the right side shows their fundamental components. The analytical air gap flux density does not show the distortion due to the slot openings, which is considered by means of the Carter factor. Moreover, it is possible to appreciate the construction of the waveform according to (12) and the distortion due to the saturation.

Low percentage errors occur in computing the no-load characteristic through the proposed procedure, with a maximum absolute value of 4.1%. Moreover, comparing the results of WFSM2 and WFSM3, the effect of neglecting the pole-to-pole leakage flux can be analysed. Specifically, slightly lower errors occur in the saturation region for lower values of k_b.

TABLE I.   MOTOR EXAMPLES FOR FEM VALIDATION.

Parameter	WFSM1	WFSM2	WFSM3
D_{so}, (mm)	250	243	243
L, (mm)	100	123	123
g_0, (mm)	0.8	1	1
p	2	3	3
q	4	3	3
k_b	0.70	0.67	0.80
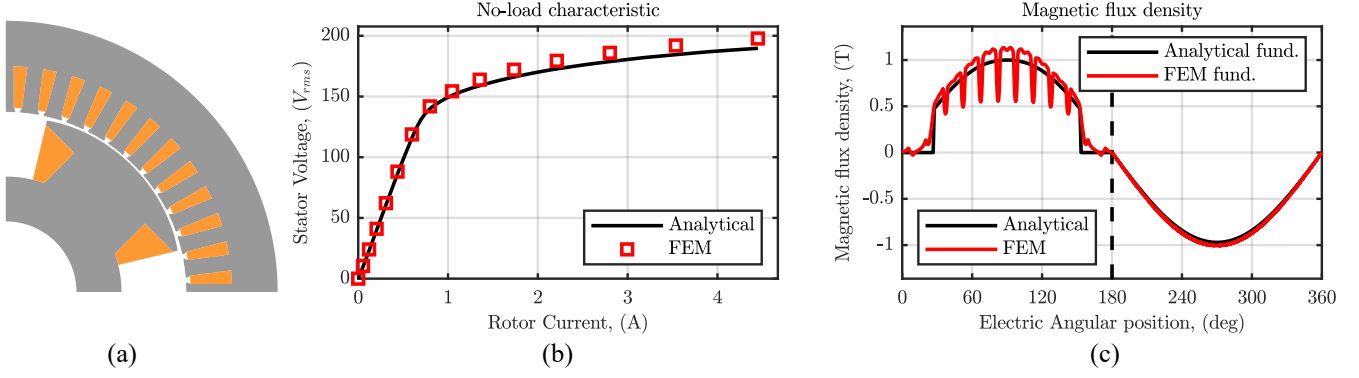
Fig. 9. Results for WFSM1: 2D sketch (a), no-load characteristic (b), air gap flux density (c).

TABLE II.   No-Load Characteristic values Comparison for WFSM1.

I_r, (A)	0.054	0.121	0.205	0.308	0.437	0.598	0.797	1.04	1.35	1.74	2.21	2.80	3.54	4.45
E_{FEM}, (V)	10.48	24.06	41.07	62.17	88.14	118.7	141.9	154.3	163.9	172.1	179.4	186.0	192.0	197.8
E_C, (V)	9.978	23.23	39.93	60.70	86.19	115.7	139.8	150.8	158.9	166.1	172.7	178.8	184.5	189.7
ϵ, (%)	-4.8	-3.5	-2.8	-2.4	-2.2	-2.5	-1.5	-2.2	-3.0	-3.5	-3.7	-3.9	-3.9	-4.1

Fig. 10. Results for WFSM2: 2D sketch (a), no-load characteristic (b), air gap flux density (c).

TABLE III.   No-Load Characteristic values Comparison for WFSM2.

| I_r, (A)	0.0551	0.124	0.209	0.315	0.446	0.610	0.813	1.07	1.38	1.77	2.26	2.86	3.61	4.54
E_{FEM}, (V)	6.017	13.71	23.33	35.30	50.14	68.43	89.79	105.7	115.5	123.0	129.5	135.3	140.5	145.4
E_C, (V)	5.760	13.27	22.75	34.57	49.23	67.26	88.11	106.0	116.2	123.3	129.3	134.7	139.9	144.5
ϵ, (%)	-4.3	-3.2	-2.5	-2.1	-1.8	-1.7	-1.9	0.24	0.67	0.19	-0.21	-0.40	-0.44	-0.61

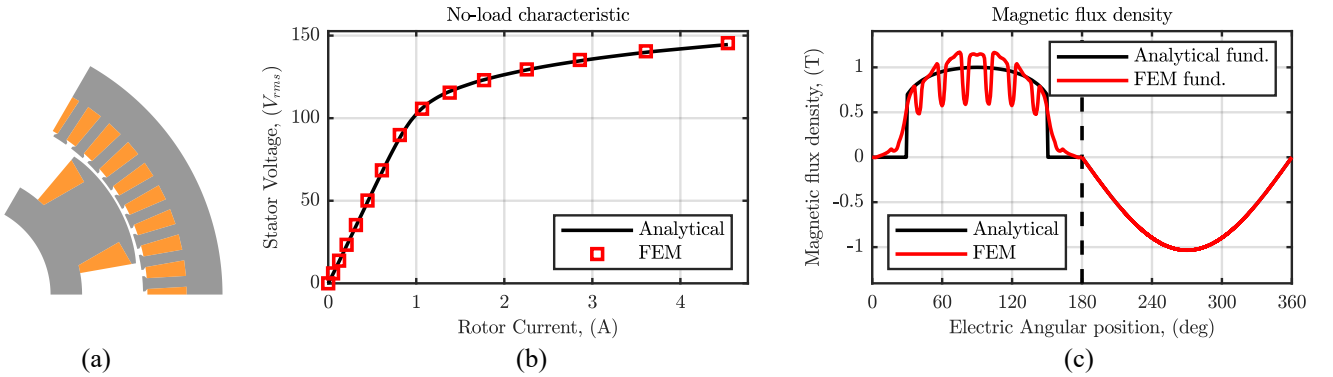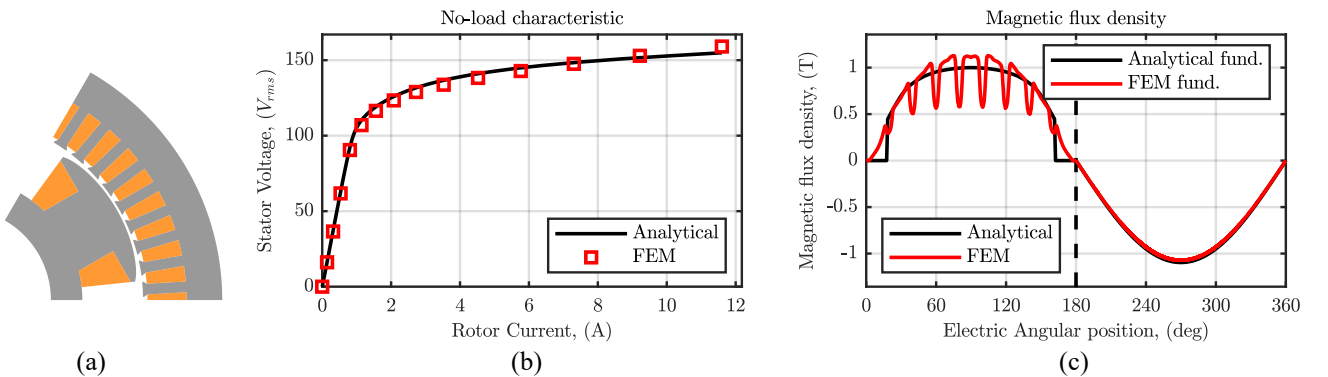

Fig. 11. Results for WFSM3: 2D sketch (a), no-load characteristic (b), air gap flux density (c).

TABLE IV.   No-Load Characteristic values Comparison for WFSM3.

I_r, (A)	0.141	0.316	0.534	0.804	1.14	1.56	2.08	2.72	3.53	4.52	5.76	7.30	9.22	11.6
E_{FEM}, (V)	16.15	36.56	61.78	90.50	107.0	116.4	123.4	128.9	133.7	138.3	142.8	147.6	152.9	159.0
E_C, (V)	16.19	37.02	62.76	92.26	110.3	119.1	125.9	131.7	136.7	141.1	144.9	148.4	151.6	154.9
ϵ, (%)	0.26	1.3	1.6	1.9	3.1	2.3	2.1	2.1	2.2	2.0	1.5	0.54	-0.83	-2.6

Fig. 12. Sample of the wound field synchronous machine.

Fig. 13. *BH*-curve measurement schematic.

B. Validation with Measurements

The proposed procedure is further validated considering as case study a salient-pole wound field synchronous motor used for traction applications. The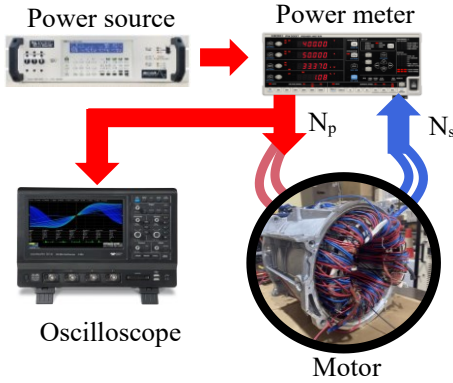 considered machine under peak performances is a 100 kW, 4-poles motor with a base speed of 4000 rpm and supplied by a 400V *dc*-link [29], [30]. The lamination geometry and the winding layout have been reversely engineered on the sample shown in Fig. 12.

The magnetic characteristic of the lamination material has been determined by experimental measurements using the test setup of Fig. 13, following the procedure reported in [31]. The stator has been equipped with two windings tightened around the stator yoke. The sample has been magnetized supplying the primary winding with an *ac* linear programmable power source capable of producing a sinusoidal voltage in the range 20Hz-5kHz with an average total harmonic distortion lower than 0.25%. The secondary winding induced voltage and the primary winding magnetizing current allow measuring the magnetization *BH* curve and the specific iron losses of the magnetic material. In order to perform the no-load test on the machine sample, the measurement setup shown in Fig. 14 has been used. The rotor of the motor under test has been kept rotating at a fixed speed (500rpm) using the prime mover, while the rotor winding has been supplied with a *dc* power source to inject the desired rotor current. The phase stator voltage has been measured for different values of the rotor current. The rotor current has been measured using the closed-loop current transducer IT200-S Ultrastab from LEM.
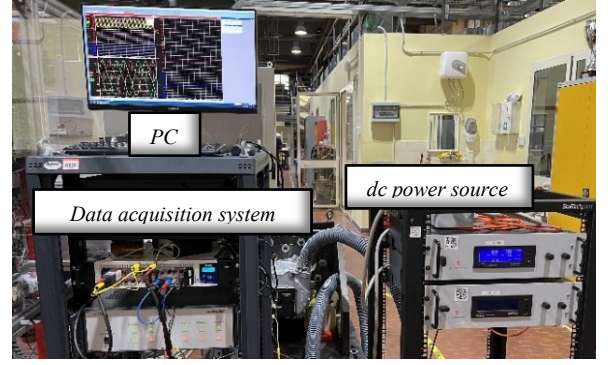
a)
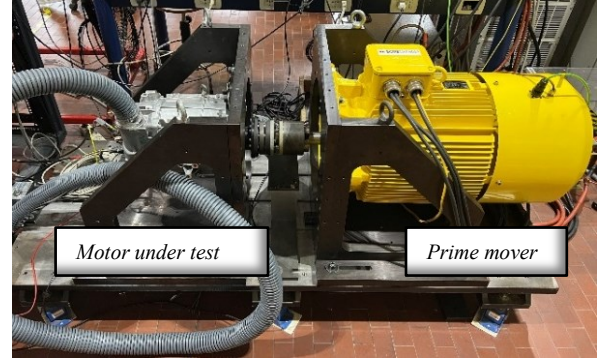
b)

Fig. 14. No-load test setup: (a) power supply, (b) test rig.

The three stator phase voltages have been measured using shielded cables connected to voltage cards GN610B from HBM Gmbh. data have been measured with a sampling frequency of 500kS/s and collected by the data acquisition system GEN2tB from HBM Gmbh. Figure 15 shows the measured stator voltages for four different rotor currents, selected from a total number of twenty tests. The measured data have been processed in order to obtain the fundamental values of the induced stator voltages, finally finding the no-load characteristic. Figure 16 shows the obtained curve, plotted in red squares. The graph also depicts the analytically computed no-load characteristic, showing a good agreement with the measured values.

To be specific, the values of the analytically computed measured characteristics are reported in Table V, with the corresponding percentage errors. The obtained values show a good analytical prediction of the no-load characteristic, with a maximum error of 5.3%. Moreover, a finite element model of the motor under analysis has been built and the resulting no-load characteristic is also shown in Fig. 16. Similarly to the FEM validations, the FE model simulated only one machine sector for a single rotor position to get the air gap magnetic flux density, while the stator voltage was computed offline through (24). The results are consistent with the measured characteristic, presenting a maximum error of 2.5%. The resulting finite element and analytical air gap flux density curves for $B_{g,max} = 1\,T$ are shown in Fig. 17. Although the analytical curve represents an approximation of the magnetic flux density in the air gap, the comparison with FEM shows an error of the fundamental value less than 3%.
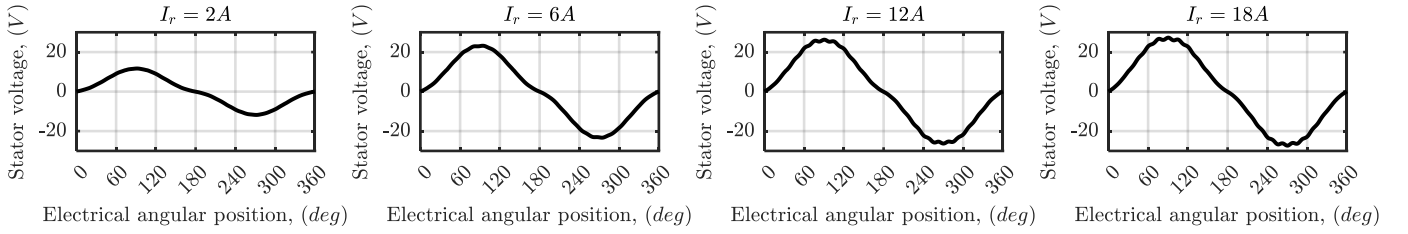
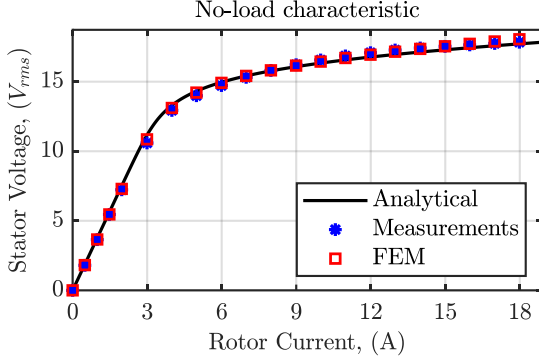Fig. 15. Measured no-load stator voltages at 500rpm for different field current excitations.
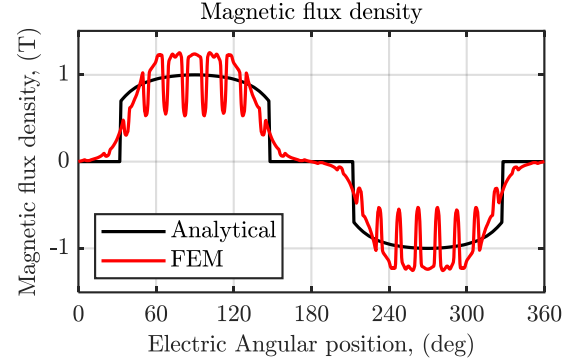

Fig. 16. No-load characteristic at 500rpm.

Fig. 17. Magnetic flux density in the air gap.

TABLE V. MEASURED AND COMPUTED NO-LOAD CHARACTERISTICS.

I_r, (A)	0.5	1.0	1.5	2.0	3.0	4.0	5.0	6.0	7.0	8.0	9.0	10.0	11.0	12.0	13.0	14.0	15.0	16.0	17.0	18.0
E_M, (V)	1.80	3.64	5.45	7.23	10.6	12.9	14.0	14.7	15.3	15.8	16.2	16.6	16.9	17.1	17.3	17.4	17.5	17.6	17.7	17.8
E_C, (V)	1.87	3.76	5.62	7.51	11.2	13.3	14.3	15.0	15.4	15.8	16.1	16.3	16.6	16.8	17.0	17.1	17.3	17.4	17.6	17.7
ϵ, (%)	3.8	3.3	3.0	3.9	5.3	2.8	2.3	1.6	0.7	-0.2	-0.9	-1.4	-1.7	-1.8	-1.9	-1.7	-1.4	-1.2	-0.9	-0.7

IV. CONCLUSION

In this paper, a fast analytical procedure for computing the no-load characteristic of wound field synchronous machines is proposed. The lamination geometry, basic winding layout information, and the magnetic characteristic of the ferromagnetic material are the required data for the computation. The algorithm considers the shunt of the stator slots, the distortion of the air gap flux density due to the iron saturation, as well as its distinctive waveform caused by the salient-pole rotor geometry of wound field machines.

The procedure has been initially validated through FEM simulations performed on three different machine geometries. The obtained results are consistent with the FEM analysis, showing a maximum percentage error of 4.1%. The proposed procedure completed the computation of a hundred of points in less than 0.5s, while the FEM simulated 15 points in approximately 1 minute in a 4-core, 3.4 GHz personal computer.

Furthermore, the procedure has been experimentally validated on a reverse engineered wound field machine sample, specifically the motor equipping the Renault ZOE. Also in this case, the results have shown a good prediction of the no-load characteristic, with a maximum error of 5.3% close to the saturation knee. The estimation errors decrease even below 1 % at high saturation operations. In this case, the proposed procedure completed the computation again in 0.5s, while the time required to complete the FEM simulations of the 20 points resulted in approximately 3 minutes.

The computational efficiency of the proposed procedure is particularly beneficial when multiple no-load characteristics need to be computed several times during the execution of optimization algorithms. Moreover, this paper provides the collection, in a single reference, of all the necessary equations to compute the no-load characteristic of wound field synchronous machines.

REFERENCES

[1] A. M. El-Refaie, "Motors/generators for traction/propulsion applications: A review," in *IEEE Vehicular Technology Magazine*, vol. 8, no. 1, pp. 90-99, March 2013.

[2] R. Thomas, H. Husson, L. Garbuio, L. Gerbaud, "Comparative study of the Tesla Model S and Audi e-Tron Induction Motors," *2021 17th Conference on Electrical Machines, Drives and Power Systems (ELMA)*, Sofia, Bulgaria, 2021.

[3] https://ec.europa.eu/info/law/better-regulation/have-your-say/initiatives/13597-European-Critical-Raw-Materials-Act_en.

[4] C. Rossi, D. Casadei, A. Pilati, M. Marano, "Wound Rotor Salient Pole Synchronous Machine Drive for Electric Traction," *Conference Record of the 2006 IEEE Industry Applications Conference Forty-First IAS Annual Meeting*, Tampa, FL, USA, 2006.

[5] D. G. Dorrell, "Are wound-rotor synchronous motors suitable for use in high efficiency torque-dense automotive drives?," *IECON 2012 - 38th Annual Conference on IEEE Industrial Electronics Society*, Montreal, QC, Canada, 2012.

[6] F. Graffeo, O. Stiscia, S. Vaschetto, A. Cavagnino, A. Tenconi, "Doubly Excited Synchronous Machines for Traction Applications," *2021 IEEE 30th International Symposium on Industrial Electronics (ISIE)*, Kyoto, Japan, 2021.

[7] S. Sakurai, T. Suwazono, "EV Traction Wound Field Synchronous Motor", EV Components, Meiden Review, Series No. 182 2021 No. 2.

[8] R. Hamidouche, S. Mezani, T. Lubin, T. Hamiti, "Analytical Model of Wound Rotor Synchronous Machine for Electric Vehicle Traction," *2022 Joint MMM-Intermag Conference (INTERMAG)*, New Orleans, LA, USA, 2022.

[9] F. Graffeo, S. Vaschetto, M. Cossale, M. Kerschbaumer, E. C. Bortoni, A. Cavagnino, "Cylindrical Wound-Rotor Synchronous Machines for Traction Applications," *2020 International Conference on Electrical Machines (ICEM)*, Gothenburg, Sweden, 2020.

[10] C. Rossi, D. Casadei, A. Pilati and M. Marano, "Wound Rotor Salient Pole Synchronous Machine Drive for Electric Traction," *Conference Record of the 2006 IEEE Industry Applications Conference Forty-First IAS Annual Meeting*, Tampa, FL, USA, 2006.

[11] J. de Santiago et al., "Electrical Motor Drivelines in Commercial All-Electric Vehicles: A Review," in *IEEE Transactions on Vehicular Technology*, vol. 61, no. 2, pp. 475-484, Feb. 2012.

[12] Y. Wang, S. Nuzzo, H. Zhang, W. Zhao, C. Gerada and M. Galea, "Challenges and Opportunities for Wound Field Synchronous Generators in Future More Electric Aircraft," in *IEEE Trans. Transportation Electrification*, vol. 6, no. 4, pp. 1466-1477, Dec. 2020.

[13] J. L. Kirtley, A. Banerjee, S. Englebretson, ``Motors for ship propulsion," *Proc. IEEE*, vol. 103, no. 12, pp. 23202332, Dec. 2015.

[14] R. Bojoi, A. Cavagnino, A. Tenconi, A. Tessarolo, S. Vaschetto, "Multiphase electrical machines and drives in the transportation electrification," *2015 IEEE 1st International Forum on Research and Technologies for Society and Industry Leveraging a better tomorrow* (RTSI), Turin, Italy, 2015.

[15] C. Bassi, A. Tessarolo, R. Menis and G. Sulligoi, "Analysis of different system design solutions for a high-power ship propulsion synchronous motor drive with multiple PWM converters," *Electrical Systems for Aircraft, Railway and Ship Propulsion*, Bologna, Italy, 2010.

[16] A.M. EL-Refaie, "Electrical Machines for Traction and Propulsion Applications," in *IEEE Transportation Electrification: Breakthroughs in Electrified Vehicles, Aircraft, Rolling Stock, and Watercraft*, 2023.

[17] J. K. Nøland, S. Nuzzo, A. Tessarolo, E. F. Alves, "Excitation System Technologies for Wound-Field Synchronous Machines: Survey of Solutions and Evolving Trends," in *IEEE Access*, vol. 7, pp. 109699-109718, 2019.

[18] A. Di Gioia, I.P. Brown, Y. Nie, R. Knippel, D.C. Ludois, J. Dai, S. Hagen, C. Alteheld, "Design and Demonstration of a Wound Field Synchronous Machine for Electric Vehicle Traction With Brushless Capacitive Field Excitation," in *IEEE Trans. Ind. Appl.*, vol. 54, no. 2, pp. 1390-1403, March-April 2018.

[19] M. Seguchi, "Self-Excited Wound-Field Synchronous Motors for xEV", *SAE Int. Journal*, Alt. Power. / Volume 6, Issue 2 (July 2017).

[20] M. L. Bash, S. D. Pekarek, "Modeling of Salient-Pole Wound-Rotor Synchronous Machines for Population-Based Design," *in IEEE Trans. Energy Conversion*, vol. 26, no. 2, pp. 381-392, June 2011.

[21] N. Tang, D. Sossong, I. P. Brown, "Design and Metamodel-Based Optimization of a High Power Density Wound Field Traction Motor," *2021 IEEE Energy Conversion Congress and Exposition (ECCE)*, Vancouver, BC, Canada, 2021.

[22] O. Laldin, S. D. Sudhoff, S. Pekarek, "An Analytical Design Model for Wound Rotor Synchronous Machines," in *IEEE Trans. Energy Conversion*, vol. 30, no. 4, pp. 1299-1309, Dec. 2015.

[23] M. Strauch, S. Dewenter, A. Binder and K. H. Nam, "Calculation of the electromagnetic characteristics of an electrically excited synchronous motor for an EV," *2012 IEEE Vehicle Power and Propulsion Conference*, Seoul, Korea (South), 2012.

[24] I. Boldea, "Synchronous Generators", 2nd edition, CRC Press, 2016.

[25] F. Graffeo, S. Vaschetto, A. Tenconi and A. Cavagnino, "No-Load Characteristic Computation for Wound Field Synchronous Propulsion Motors," *2023 IEEE International Conference on Electrical Systems for Aircraft, Railway, Ship Propulsion and Road Vehicles & International Transportation Electrification Conference (ESARS-ITEC)*, Venice, Italy, 2023.

[26] J. Pyrhonen, T. Jokinen, V. Hrabovcova, "Design of Rotating Electrical Machines", 2nd edition, Wiley, 2014.

[27] A. Boglietti, A. Cavagnino, M. Lazzari, "Computational Algorithms for Induction Motor Equivalent Circuit Parameter Determination—Part II: Skin Effect and Magnetizing Characteristics," in *IEEE Trans. Ind. Electron.*, vol. 58, no. 9, pp. 3734-3740, Sept. 2011.

[28] D. Meeker, "FEMM: Finite Element Method Magnetics." [Online]. Available: www.femm.info

[29] F. Graffeo, S. Vaschetto, A. Tenconi and A. Cavagnino, "Fast Sizing Procedure for Salient-Pole Wound Field Synchronous Motors for Transportation Electrification," *2023 IEEE International Electric Machines & Drives Conference (IEMDC)*, San Francisco, CA, USA, 2023.

[30] "RENAULT ZOE E-TECH 100% electric," accessed: 29-March-24. [Online]. Available: https://cdn.group.renault.com/ren/gb/transversal-assets/brochures/mobile-brochure-tech-spec/mobile-tech-spec-zoe.pdf

[31] S. Vaschetto, Z. Gmyrek, C. Dobler, G. Bramerdorfer and A. Cavagnino, "Experimental Assessment and Modeling of Losses in Interlocked Magnetic Cores," in *IEEE Trans. Ind. Appl.*, vol. 58, no. 4, pp. 4450-4460, July-Aug. 2022.

Federica Graffeo (Member, IEEE) received the B.Sc. degree in Energy Engineering from Università degli Studi di Palermo (Italy) in 2017, the M.Sc. and Ph.D. degree in Electrical Engineering from Politecnico di Torino (Italy) in 2020, and 2023, respectively. She is currently Assistant Professor with Dipartimento Energia "G. Ferraris," Politecnico di Torino. She serves as a reviewer for some IEEE Transactions and international conferences. Her main research interests include electromagnetic and thermal design of synchronous electrical machines for transportation applications, with a particular focus on wound field synchronous motors.

Silvio Vaschetto (Senior Member, IEEE) received the M.Sc. and Ph.D. degrees in electrical engineering from the Politecnico di Torino, Italy, in 2007 and 2011, respectively. He then joined ABB IEC LV Motors Technology Center, Vittuone, Italy as R&D engineer. From 2012 to 2014 he was with Magna Electronics Italy, as Electromagnetic Simulation and Motor Design Engineer. He is currently an Associate Professor at the Energy Department "G. Ferraris", Politecnico di Torino. His research interests include electromagnetic design, thermal analysis, and energetic behavior of electrical machines for transportations and high-performance applications. He is an Associate Editor for IEEE Transactions on Industry Applications, IEEE Transactions on Energy Conversion and Special Issues Editor for IET Electric Power Applications Journal.

Sandro Rubino (Member, IEEE) received the M.Sc. and Ph.D. degrees in Electrical Engineering from Politecnico di Torino, Torino, Italy, in 2014 and 2019, respectively. He is currently Assistant Professor with Dipartimento Energia "G. Ferraris," Politecnico di Torino. He serves as a reviewer for some IEEE Transactions and international conferences. His main research interests include power electronics, modeling, and control of multiphase electrical machines and high-performance ac motor drives. Dr Rubino is an Associate Editor of IEEE Transactions on Industry Applications on behalf of the Industrial Drive Committee of the IEEE Industry Applications Society. He was the recipient of two paper awards from the Industrial Drives Committee of the IEEE Industry Applications Society and two Ph.D. thesis awards from the IEEE Power & Energy Society Italy Chapter and the IEEE Industrial Electronics Society Italy Chapter, respectively.

Alberto Tenconi (Senior Member, IEEE) received the M.Sc. and Ph.D. degrees in electrical engineering from the Politecnico di Torino, Torino, Italy, in 1986 and 1990, respectively. From 1988 to 1993, he was with the Electronic System Division, FIAT Research Center, where he was engaged in the development of electrical vehicle drive systems. He then joined the Department of Electrical Engineering (now Energy Department), Politecnico di Torino, where he is currently head of Department. His research activity is documented by more than 200 papers published in International Journals and International Conferences. He has participated, both as a designer and as scientific responsible, in many National and European Research Programmes. He is a reviewer for International Journals and has been Associate Editor for the Transactions on Industrial Electronics. His current research interests include electric machines, power converters and drives for transportation electrification.

Andrea Cavagnino (Fellow, IEEE) received his M.Sc. and Ph.D. degrees in electrical engineering from the Politecnico di Torino, Italy, in 1995 and 2000, respectively. He is a professor at the Politecnico di Torino. He has authored or co-authored more than 260 papers, receiving four Best Paper Awards. His research interests include electromagnetic design, thermal design, and energetic behaviour of electrical machines. He usually cooperates with factories for a direct technological transfer and he has been involved in several public and private research projects. Prof. Cavagnino is an Associate Editor of the IEEE Transactions on Energy Conversion (TEC), a Past Chair of the Electrical Machines Technical Committee of the IEEE Industrial Electronics Society, a past Associate Editor of the IEEE Transactions on Industrial Electronics (TIE), and the IEEE Transactions on Industry Applications. He was also a Guest Editor of six Special Sections for IEEE-TIE and co-Editor in Chief of a Special Issue for IEEE-TEC. Prof. Cavagnino was a technical program chair of the IEEE-IEMDC 2015, IEEE-ECCE 2022 and IEEE-ECCE 2025 conferences. He is a reviewer for several IEEE Transactions and other international journals and conferences.